RESEARCH ARTICLE

[M]acro-
[M]olecular
Materials and Engineering
Open Access
www.mame-journal.de

Ion Track Formation and Nanopore Etching in Polyimide: Possibilities in the MeV Ion Energy Regime

Rajdeep Kaur,* Ghada Eljamal, Tuan Thien Tran, Daniel Primetzhofer, and Petter Ström

Polyimide films of thickness 7.5 µm are irradiated by a wide range of ions (^{1}H to ^{197}Au) with energies between 1.05 and 48 MeV. Irradiated samples are then chemically etched in sodium hypochlorite solution to investigate nanopore formation due to ion track etching. A threshold in terms of electronic stopping power, S_{et}, needs to be surpassed to preferentially etch the ion tracks. Close to S_{et}, intermittent tracks are formed where only part of the track is etchable. The fraction of these etchable parts increases as we move away from S_{et}, toward higher stopping powers, eventually yielding continuous etchable tracks. Both intermittent and continuous track formation thresholds are observed to be velocity-dependent, yielding a decrease of the thresholds in the present work compared to previously reported thresholds for swift heavy ions. This finding leads the authors to suggest that electrostatic ion accelerators with terminal voltages of several MV are applicable for the production of ion track membranes up to ≈10–20 µm in thickness. Suitable ions for nanopores in 7.5 µm polyimide films include 42 MeV ^{59}Co and 48 MeV ^{197}Au. The growth mechanism for the pores during etching is discussed, relating it to the properties of the original ion track.

1. Introduction

Inspired by biological nanoscale pores and channels, solid-state nanoporous membranes have shown great potential in a wide range of applications such as gas/ion detection and separation,[1,2] DNA/RNA detection and sequencing,[3,4] selective drug delivery,[5] water desalination,[6] and sensors.[7–9] When a nanoporous membrane is immersed in an electrolyte solution
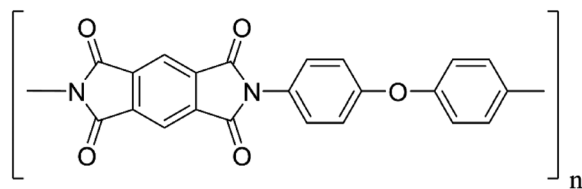
R. Kaur, G. Eljamal, T. T. Tran, D. Primetzhofer, P. Ström
Department of Physics and Astronomy
Applied Nuclear Physics
Uppsala University
Uppsala 751 20, Sweden
E-mail: rajdeep.kaur@physics.uu.se
D. Primetzhofer
Tandem Laboratory
Uppsala University
Uppsala 751 21, Sweden

and a suitable voltage is applied across the membrane, an ion current flows through the pores. Nanopore detection and sequencing work on the principle of ionic current disruption or variation. Several insulating materials, for example, graphene,[6,10] silicon nitride,[11,12] silicon oxide,[13,14] and polymer membranes[7,15–17] are being studied for nanoscale channel and pore fabrication. Although silicon-based nanopores allow improved miniaturization and possible integration with other electronic devices, the irregular shape of these pores leads to large current noises.[18] Among polymers, pores in polyimide (PI) are reported to have very stable current signals.[19] Additionally, PI exhibits strong chemical resistance as it is insoluble in almost all organic compounds; has heat stability over a wide range of temperatures ranging from −269 to 400 °C, and has excellent mechanical strength, making it a very suitable candidate for fabrication of practical nanoporous components.

Many studies have been conducted on the formation of tracks that may be chemically etched to create nanopores in PI after irradiation with swift heavy ions (SHI), where typical ion energies have been on the order of a few MeV u^{-1}.[20–23] A threshold in terms of energy deposited by the ions on the target electronic system per unit path length (electronic stopping power, S_e) is reported as 1.85 keV nm^{-1} for the formation of intermittent tracks and 5 keV nm^{-1} for continuous tracks.[20] However, Yamauchi et al. reported that the threshold for formation of etchable tracks in PI is not constant but depends on the ion and it can be related to the breaking of two adjacent diphenyl ether bonds in the PI chains.[21] Based on the energy required to break diphenyl ether bonds, the threshold for the formation of these tracks is inferred as 2.5 keV nm^{-1}. Sodium hypochlorite (NaOCl) solution preferentially dissolves ion-damaged areas to form pores. The bulk etch rate (V_B) and track etch rate (V_T), and thus, the shape of the pores depends on the conditions such as temperature, active chlorine content, and pH of NaOCl solution. The V_B of PI in NaOCl is reported to increase exponentially with pH while V_T remains almost constant with pH, leading to the formation of cylindrical pores for pH < 11 and conical pores for higher pH.[22,23] The literature reports a detailed analysis of V_B, V_T, and pore shape in PI based on pH and active chlorine content in NaOCl solution.[22,24]

Given the great interest in developing solid-state nanopores for different applications,[1,3,5–7,9,15] the ability to reproduce nanopores by lower energy ($E < 1$ MeV u^{-1}) ion irradiation can prove helpful in the possible commercialization of nanopore fab-

ADVANCED SCIENCE NEWS
www.advancedsciencenews.com

[M] acro- olecular Materials and Engineering
Open Access
www.mame-journal.de

Figure 1. Monomer unit of Kapton based on Figure 1 in ref. [23].

rication in the future. The penetration range of such ions is lower than SHI, but for some applications, for example: single DNA molecule detection,[3,4] protein biosensors,[8] single porphyrin molecules detection,[25] and ion separation;[1] a few micrometers long pores are sufficient, which can be easily achieved using ion energies of a few MeV. In the present work, we focus on investigating the formation of nanopores in polyimide by irradiation with these less-explored and more accessible MeV ions. Self-supporting PI films were irradiated by ions with a wide range of mass (^{1}H to ^{197}Au) to investigate the threshold value for ion track formation. The latent tracks thus created were etched out using NaOCl to form nanopores. The threshold value for the formation of intermittent as well as continuous tracks in terms of S_e and the effect of projectile velocity on these threshold values are investigated. Directional effects of the incident ion on the formation of ion track in PI films are also studied by irradiating stacked films.

2. Experimental Section

2.1. Ion Irradiation

Commercially available Kapton 30EN polyimide films with a thickness of 7.5 μm, delivered by DuPont, were used in the present work. The monomer unit of Kapton (poly(4,4′-oxydiphenylene) pyromellitimide) is shown in **Figure 1**. The films of area 4×4 cm^2 were irradiated at room temperature under normal incidence by ^{1}H, ^{12}C, ^{16}O, ^{28}Si, ^{59}Co, and ^{197}Au ions with

energies ranging from 1.05 to 48 MeV and an initial charge state between 1+ and 11+. Beam current was measured before and after irradiation using a Faraday cup placed behind the sample position. The beam was scanned using ±10 kV deflection voltage with a frequency of 64 Hz in the horizontal and 517 Hz in the vertical direction to deliver a homogeneous current density of $(4 \pm 1) \times 10^{-3}$ nA cm^{-2} over the entire film. Low ion fluences of $(1.0–5.0) \times 10^8$ ions cm^{-2} were used for most of the irradiations to avoid overlapping nanopores. Some of the samples were also irradiated with a higher fluence of 1.0×10^{10} ions cm^{-2} to analyze the irradiated films that were either unetched or etched for only 15 min.
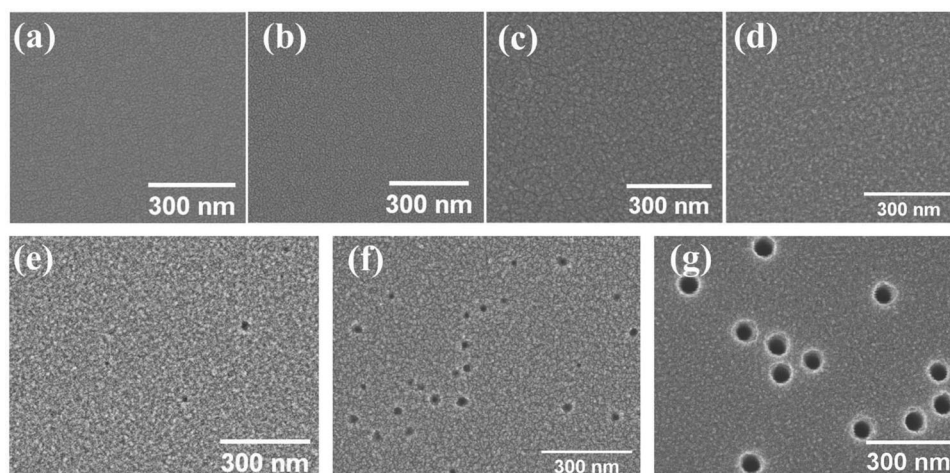
All the irradiations were performed using a 5 MV pelletron tandem accelerator at Uppsala University.[26] **Table 1** compiles a complete list of the kinetic energy (E_K), specific kinetic energy, S_e at equilibrium charge state (q_{eq}) for initial energy, initial charge (q_{in}), and range (R_p) of the projectiles used to irradiate the polyimide films. The electronic stopping power (S_e), range (R_p), and energy of the ions transmitted (E_T) through the film were calculated using SRIM-2013,[27] and q_{eq} was calculated using the formula for solid-state targets from the literature.[28] All the projectile ions (except ^{1}H ions) used in this work have $q_{in} < q_{eq}$. The charge state equilibration length, d,[29] for the ions used in this work, is 5 ± 2 nm. Comparing these values with the reported bulk etching rate of a few tens of nm h^{-1} in the literature,[23] it was assumed that surface structures observed after a few hours of etching would have a minimal effect of the fact that q_{in} was different from q_{eq}. Thus, the S_e calculated at q_{eq} can be used for the analysis of the threshold for nanostructure formation in this work.

2.2. Wet Chemical Etching

The irradiated PI films of area 1×1 cm^2 were symmetrically etched from both sides in an aqueous NaOCl solution kept at (50 ± 1) °C. The pH was measured using a digital pH meter and chlorine content was determined indirectly by a standard

Table 1. List of the projectiles used for irradiating 7.5 μm thick PI films with their kinetic energy (E_K), specific kinetic energy, electronic stopping power (S_e) at equilibrium charge state (q_{eq}) for initial energy, initial charge (q_{in}) and range (R_p). S_e and R_p were calculated using SRIM-2013.[27]

Ion	E_K [MeV]	Specific E_K [MeV u^{-1}]	S_e [keV nm^{-1}]	q_{in}	Range [μm]	Ion	E_K [MeV]	Specific E_K [MeV u^{-1}]	S_e [keV nm^{-1}]	q_{in}	Range [μm]
^{1}H	1.05	1.05	0.03	1+	21.2		11	0.39	2.83	3+	6.3
	2	2	0.02	1+	58.7		18	0.64	2.99	5+	8.7
^{12}C	2.75	0.23	1.04	1+	3.9	^{59}Co	2	0.034	0.88	1+	2.1
	4.5	0.375	1.08	2+	5.6		4	0.068	1.56	3+	3.5
	7	0.58	1.04	3+	7.9		5	0.085	1.91	3+	4.1
^{16}O	2	0.125	1.16	1+	2.9		9	0.15	3.10	3+	5.6
	3.25	0.2	1.40	1+	3.9		17	0.29	4.43	3+, 7+, 9+	7.6
	6.5	0.41	1.54	3+	6.1						
	13	0.81	1.40	3+	10.4		37	0.63	5.55	9+	11.5
	16	1	1.33	4+	12.6		42	0.71	5.66	9+	12.4
	24	1.5	1.16	6+	19.1	^{197}Au	5	0.025	1.96	3+	1.5
^{28}Si	2	0.07	1.33	1+	2.3		12	0.061	2.18	4+	5.5
	4	0.14	1.94	2+	3.5		42	0.21	5.56	9+	11.2
	5	0.18	2.16	3+	4.0		48	0.24	6.32	11+	12.2

Figure 2. SEM images for a) unirradiated and unetched, b) irradiated (42 MeV Au^{9+}) but unetched, and c) unirradiated but etched PI film; films irradiated with d) 1.05 MeV H$^+$, e) 16 MeV O^{4+}, f) 6.5 MeV O^{3+}, and g) 42 MeV Au^{9+}. All films (except [a and b]) were etched for 4 h. Fluence for all irradiations (except for [b], which was irradiated with a fluence of $[1 \pm 0.3] \times 10^{10}$ ions cm^{-2}) was $(5 \pm 1.3) \times 10^8$ ions cm^{-2}.

iodine/thiosulphate titration method.[30] The pH of the as-purchased NaOCl solution was ≈12 ± 0.2 and the initial Cl content was between 7.8% and 9.75% w/v. The pH of the solution was adjusted to 10 using a 10% v/v hydrochloric acid (HCl) solution. Under these etching conditions, either cylindrical[23] through pores or conical partial pores/pits were expected to be formed in the irradiated PI film. Most of the PI films were etched for 4 h. It was observed that the pH of the solution slowly decreased by ≈5% after 4 h of etching and the chlorine content was reduced by ≈2% on average. The changes were due to the degradation of the hypochlorite at elevated temperatures.[31] For longer etching experiments, the PI films were immersed in fresh NaOCl solution every 4 h. After etching, the films were washed several times with deionized water to neutralize the surface and remove the residual salts.

The etching time (T_E) was varied from 15 min to 8 h for three irradiation conditions, viz. films irradiated with 5 MeV Co^{3+}, 17 MeV Co^{7+}, and 37 MeV Co^{9+}. These films were used to study the dependence of the pore size on T_E, and thus, extract the pore growth rate both radially and in the direction of the latent ion track.
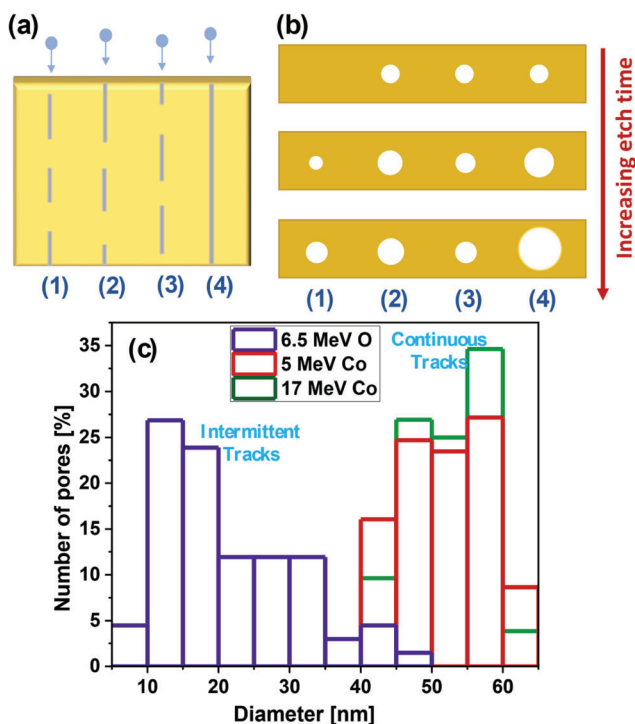
2.3. Characterization

The thickness of two as-purchased PI films and four unirradiated films etched for 10, 32, 60, and 77 h, respectively was measured with proton elastic backscattering spectrometry (EBS), to estimate the material bulk etch rate (V_B). The measurements were performed using a 2 MeV p$^+$ beam with a detector placed at a backscattering angle of 170°. The experimental EBS spectra were fitted using SIMNRA 7.03[32] to calculate the film thickness and subsequently derive the bulk etch rate. The weight and dimensions of each film were also measured before and after the etching using a laboratory scale of least count 0.1 mg and a meter scale of least count 0.05 cm respectively.

The surface characterization of the irradiated polyimide films was done using Zeiss LEO 1550 and Zeiss LEO 1530—scanning electron microscopy (SEM) at an acceleration voltage of 10 kV, and PSIA XE150 atomic force microscopy (AFM). To observe the cross-section of the nanopores, one of the samples was studied by transmission electron microscopy (TEM). TEM lamellae were cut out of the film by Zeiss FIB/SEM Crossbeam 550 with Ga Ion-Sculptor gun and analysis was conducted with a FEI Titan Themis 200 system at an acceleration voltage of 200 kV. The films were coated with a thin layer of Au–Pd using a Polaron SC7640 sputter coater to prevent charging of the films during SEM measurements and lamella preparation. An additional layer of Pt, initially using an electron gun and then with a Ga ion gun, was coated over the films before cutting out the lamella. This preparation was done to prevent the region of interest below the Pt layers from getting damaged during cutting. SEM and TEM image processing was performed using ImageJ[33] and AFM image processing was performed using Gwyddion.[34]

3. Results and Discussion

Figure 2 shows the SEM images for a) pristine (i.e., unirradiated and unetched), b) irradiated (42 MeV Au^{9+}) but unetched, c) unirradiated but chemically etched PI film; the films that were etched after irradiation with d) 1.05 MeV H$^+$, e) 16 MeV O^{4+}, f) 6.5 MeV O^{3+}, and g) 42 MeV Au^{9+}. All the films were etched in NaOCl solution for 4 h at 50 °C after irradiation, if not specified otherwise. No significant surface modification or nanostructure formation is observed for the irradiated but unetched film (Figure 2b), indicating that chemical etching is an essential step to create observable nanostructures in PI films in the energy regime studied in this work. This observation is further corroborated by AFM investigation of the irradiated but unetched film, indicating no significant surface modification. The SEM images of the surface of the ion-irradiated and etched PI films show different amount of damage on the surface depending on the properties of the projectile ion. In Figure 2d, the surface is similar to Figure 2c indicating that the 1.05 MeV H$^+$ ions did not cause any clearly visible damage to the PI film, whereas nanopits or pores are observed in Figure 2e–g. The pits

**ADVANCED
SCIENCE NEWS**

www.advancedsciencenews.com

[M] acro-
olecular
Materials and Engineering
Open Access

www.mame-journal.de

Figure 3. a) Schematic for intermittent or continuous tracks which may be formed after irradiating PI film with different ions (etchable part of the tracks is shown with grey lines); b) The qualitative relative size of the nanopits or pores as expected to appear in SEM image for tracks (1–4) with increasing etch time; c) Opening diameter distribution for PI films irradiated with 6.5 MeV ^{16}O (S_e = 1.5 keV nm^{-1}), 5 MeV ^{59}Co (S_e = 1.9 keV nm^{-1}), and 17 MeV ^{59}Co (S_e = 3.1 keV nm^{-1}), and etched for 4 h at 50 °C.

observed in Figure 2e,f have a wide opening size distribution. The size distribution becomes narrower in Figure 2g where we also observe nanopores rather than what appear to be shallow pits (see also Figure 10). The areal number density of etched-out structures observed in Figure 2e is very low (<30% of fluence of the incident ions) as compared to those observed in Figure 2f,g. The ion impacts on the sample surface are stochastically distributed. As a result, some of the areas have a higher number of ion impacts compared to other areas on the sample surface. SEM images for the areas with a higher number of impacts were chosen to have a better view of the pores formed on the surface. Thus, some of the SEM images (e.g., Figure 2f) seem to suggest a fluence much higher than the fluence of incident ions.

We propose that the nanopits (Figure 2e,f) with wide size distribution observed on the surface are a sign of the formation of intermittent tracks in the film which can be attributed to the stochastic nature of damage creation along the trajectory of an ion.[20] This proposed mechanism is illustrated in **Figure 3**, where subfigure (a) shows a few examples of possible tracks formed after irradiating PI film with different ions. Etchable parts of the tracks are marked with grey lines. A qualitative sequence of relative opening sizes of the nanopits or pores as expected to appear in the SEM image for the tracks is shown in Figure 3b. The opening diameter depends on the etching time, the length of the etchable part of the tracks, and the depth of the etchable tracks

from the surface. For example, the etchable part of tracks (2) to (4) starts on the surface while the etchable part of track (1) starts at a certain depth inside the film. Thus, for short etching time, all but track (1) are initially exposed to the etchant, leading to similar opening diameters corresponding to all but track (1). On further etching, track (1) is also exposed to etchant leading to a pore opening while the opening diameter for other tracks grows depending on the length of their initial etchable parts. Thus, after intermediate etching time, track (3) does not show any significant change in opening diameter while the diameter for track (2) grows, but not as prominently as for track (4). For a long enough etching time, the opening diameter might be described as some function of the fraction of the etchable part of the ion track. Thus, the distribution of opening diameter can be used as a parameter to classify the tracks formed in the PI film into continuous and intermittent. PI film irradiated with 6.5 MeV ^{16}O has an opening diameter ranging from 5 to 50 nm (Figure 2f) while that irradiated with 42 MeV ^{197}Au has an opening diameter ranging from 45 to 60 nm (Figure 2g), indicating that the ion tracks formed in the former film have a very large variation in the fraction of etchable part of the track. The opening diameter distribution curves for 6.5 MeV ^{16}O (S_e = 1.5 keV nm^{-1}), 5 MeV ^{59}Co (S_e = 1.9 keV nm^{-1}), and 17 MeV ^{59}Co (S_e = 3.1 keV nm^{-1}) in Figure 3c also show that the opening diameter distribution at lower S_e is almost two times larger than at the higher S_e. About 60–80 pores were evaluated for the distribution curve in Figure 3c.

Based on the opening diameter distribution studied on the surface of the PI film, three different regions of ion damage are identified and plotted in **Figure 4** as a map of the specific energy and S_e of the incoming projectiles used in this work. As the films were symmetrically etched from both sides, points corresponding to the transmitted ions where the range of the ion is greater than the thickness of the film, that is, 7.5 μm are also included. The transmitted ions have a distribution of energy that can be attributed to energy-loss straggling and was determined via SRIM simulation. Thus, for points referring to transmitted ions, the average of this energy distribution along with the corresponding S_e was added to Figure 4. The three regions identified are: region (I) where no etchable ion tracks are formed; region (II) where intermittent tracks resulting in etched structures with a wide opening size distribution are formed (diameter ranging from 5 to 50 nm as shown for 6.5 MeV ^{16}O in Figure 3c); and region (III) where continuous tracks with a relatively small distribution in pore opening diameter are formed after etching (diameter ranging from 45 to 65 nm as shown for 5 and 17 MeV ^{59}Co in Figure 3c). Due to the stochastic nature of damage creation along an ion trajectory, the borders between the three regions are not sharp. Thus, region (I) is defined to include points where no etchable pore is observed in SEM images, and region (III) is defined to include points where the standard deviation in diameter ≤6 nm and areal density of the etched-out structures is within ±30% of the fluence of incident ions. The rest of the points are included in region (II). In Figure 3c, the distribution curve for 6.5 MeV ^{16}O (diameter = 21.4 ± 9.7 nm) represents a typical opening diameter distribution for ions in region (II) while distribution curves for 5 and 17 MeV ^{59}Co (diameter = 52 ± 6 and 53 ± 5 nm, respectively) represent typical opening diameter distributions for ions in region (III).
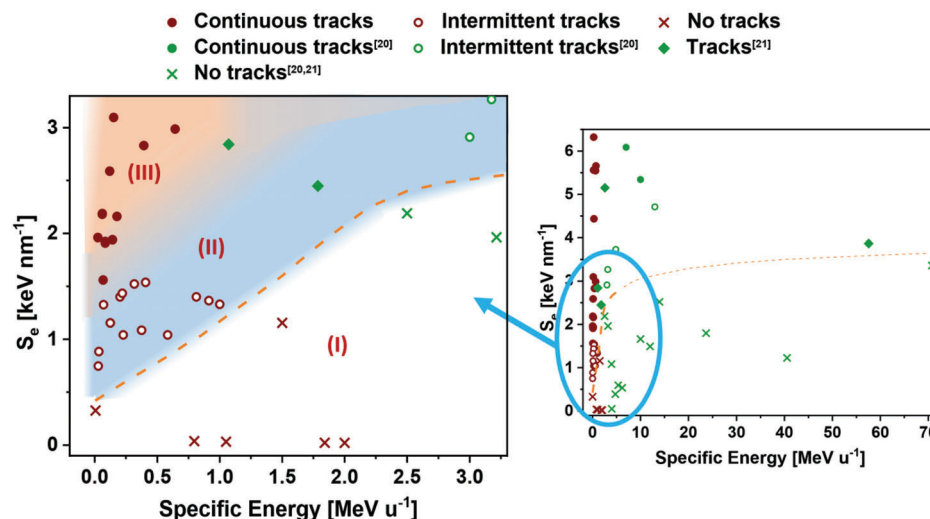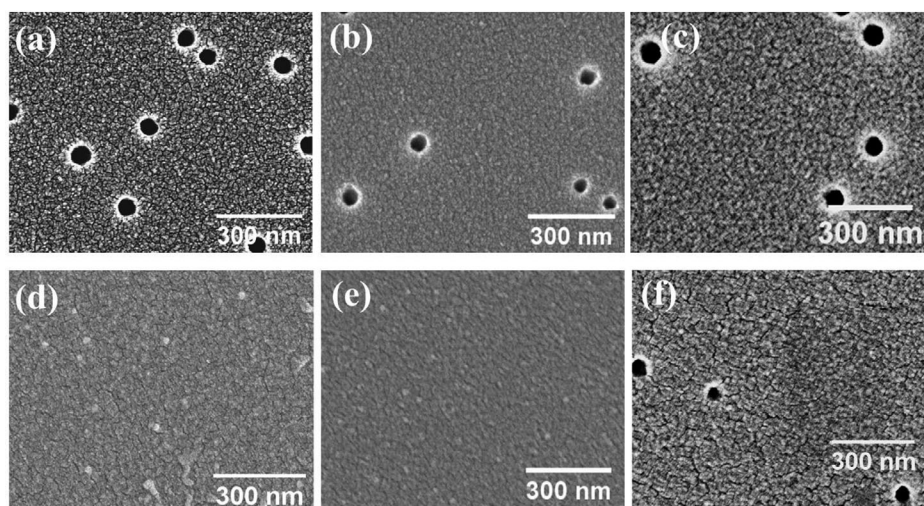
Figure 4. Region (I): crosses indicate projectiles for which no etchable ion tracks are formed (Figure 2d); Region (II): hollow circles indicate projectiles for which intermittent tracks were formed resulting in etched nanopits with wide opening size distribution (Figure 2e,f); Region (III): solid circles indicate projectiles for which continuous tracks were formed resulting in etched nanopores with relatively smaller opening diameter distribution (Figure 2g). Points from the present work are in maroon color while points from the literature for PI films of thickness 25,[20] 50,[20] and 125[21] μm are in green color. Ref. [21] does not specify whether the tracks were intermittent or continuous and are thus represented by solid rhombi. The orange dashed line is drawn as a rough line dividing regions (I) and (II).

For projectiles in the region (I), the energy deposited is not enough to create the damage required for preferential etching of pores (Figure 2d). Thus, a certain damage threshold in terms of electronic stopping power, S_{et}, is required to produce an etchable ion track in PI. $S_{et} \approx 0.5 \pm 0.2$ keV nm^{-1} is observed for the ions with energy ≈0.02 MeV u^{-1}. But for ions with energy 1.5 MeV u^{-1}, no etched-out structures are observed for S_e as high as 1.16 keV nm^{-1}. Thus, the value of the S_{et} is not constant but increases with the specific energy of the projectile, which can be attributed to the "velocity effect," referring to the dependence of the energy density deposited in the target on the velocity of the ions.[35] For the same S_e, energy is deposited into a larger radius for higher velocity ions and consequently, the deposited energy density in the target is lower and can vary up to one order of magnitude.[36] Thus, a higher value of S_e is required to create the same type of damage with higher velocity ions. In the ion energy regime employed for the present work, the velocity effect on the threshold for nanostructure formation is also observed for other materials, like CaF$_2$.[37,38] For 7 MeV ^{12}C (Specific energy = 0.58 MeV u^{-1}; S_e = 1.04 keV nm^{-1}) and 16 MeV ^{16}O (Specific energy = 1 MeV u^{-1}; S_e = 1.33 keV nm^{-1}), only a few tens of etched-out structures are found over the entire irradiated area of 1×1 cm^2 (fluence of irradiation was 5×10^8 ions cm^{-2}), indicating that we are very close to S_{et} at these points. Additional points from the literature[20,21] were added to Figure 4 to verify that the trend in S_{et} extends to higher ion velocities. As observed in Figure 4, the velocity effect is more dominant for $E < 2$ MeV u^{-1} and the effect becomes less prominent with an increase in ion velocity. The rate of increase in S_{et} with specific energy is ≈100 times larger for projectiles with $E < 2$ MeV u^{-1} than for projectiles with $(30 < E < 70)$ MeV u^{-1}. Above S_{et}, in region (II), intermittent tracks are formed and these tracks feature larger and larger etchable fractions when approaching region (III), in which tracks are considered continuous and are etched through the entire film. A second threshold in terms

of electronic stopping power, $S_{et}{}^c$, is found that divides regions (II) and (III). $S_{et}{}^c \approx 1.4 \pm 0.1$ keV nm^{-1} is observed for ions with energy ≈0.07 MeV u^{-1}. But for ions with energy 1.5 MeV u^{-1} and $S_e \approx 1.4 \pm 0.1$ keV nm^{-1}, a wide distribution of opening diameter (indicating intermittent tracks) is observed. This implies that the velocity effect is also present for $S_{et}{}^c$, for projectile ions with $E < 2$ MeV u^{-1}.

Figure 5 shows SEM images for the a–c) front and d–f) back side of PI films irradiated with a,d) 5 MeV Co^{3+}, b,e) 17 MeV Co^{3+}, and c,f) 37 MeV Co^{9+}, and chemically etched for 4 h at 50 °C. No nanopits or pores are observed in Figure 5d as the range of the projectile ion, that is, 4.1 μm is shorter than the thickness of the film. In the case of 17 MeV Co^{3+} (Figure 5e), although the range of the ions is 7.6 μm, the average energy of the transmitted ions is 0.4 ± 0.2 MeV with an associated S_e (≈0.3 ± 0.1 keV nm^{-1}) below the S_{et}, and thus, no nanopits are observed in this case either. In the case of 37 MeV Co^{9+} (Figure 5f), the transmitted ions have an average energy of 5 ± 0.3 MeV with an associated S_e (≈1.9 ± 0.1 keV nm^{-1}) above the S_{et}. This energy was verified to be within ±20% by direct measurement using a PIPS detector placed behind the membrane. In this case, the average opening diameter on the front side is larger and the size distribution is narrower than on the back side of the film. As both sides were subjected to the same etching conditions at the same time, the bulk etch rate on both sides is not subjected to any changes. The difference in the distribution of opening diameter can be attributed to the fact that the transmitted ions have energy ranging from 1.7 to 5.5 MeV (calculated using SRIM) with corresponding S_e ranging from 0.8 to 2.1 keV nm^{-1} that spreads these transmitted ions in the region (II) and (III).

The effect of directionality of projectile ions is studied by irradiating a pair of films stacked together and irradiated with an initial energy of 24 MeV O^{6+} and the schematic of the set-up is shown in **Figure 6**a. The films were stacked together with no space in

ADVANCED
SCIENCE NEWS
www.advancedsciencenews.com

Macro-
molecular
Materials and Engineering
Open Access
www.mame-journal.de

Figure 5. SEM images for films irradiated with a) 5 MeV Co^{3+} (Front), b) 17 MeV Co^{3+} (Front), c) 37 MeV Co^{9+} (Front), d) 5 MeV Co^{3+} (Back: No transmitted ions), e) 17 MeV Co^{3+} (Back: Energy of transmitted ions $\approx 0.4 \pm 0.2$ MeV), f) 37 MeV Co^{9+} (Back: Energy of transmitted ions $\approx 5 \pm 0.3$ MeV). All films were irradiated with a fluence of $(1 \pm 0.3) \times 10^8$ ions cm^{-2} and etched in NaOCl for 4 h at 50 °C.
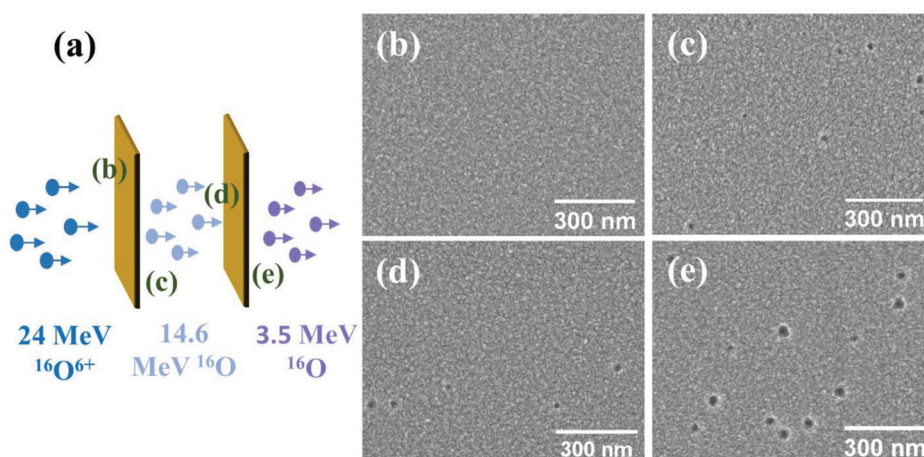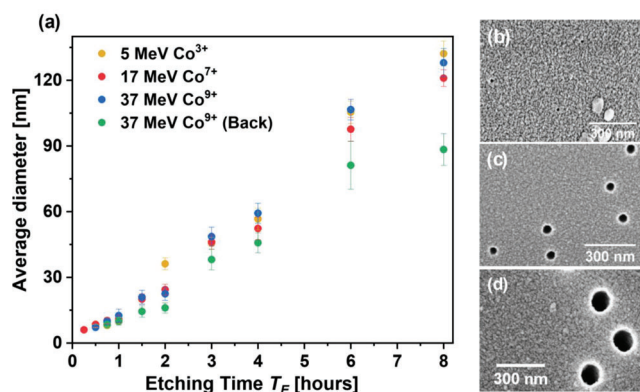

Figure 6. a) Schematic for a pair of films stacked together during irradiation. The films were stacked with no spacing between the layers. The space in the schematic is shown to illustrate the back side of the layer I and the front side of the layer II separately. SEM images for films irradiated with 24 MeV ^{16}O^{6+} and etched in NaOCl for 4 h at 50 °C: b) front side of layer I, c) back side of layer I (Energy of transmitted ions $\approx 14.6 \pm 0.2$ MeV), d) front side of layer II, and e) back side of layer II (Energy of transmitted ions $\approx 3.5 \pm 0.1$ MeV).

between but the space in the schematic is shown to illustrate the back side of the first layer and the front side of the second layer separately. No nanopits or pores are observed on the front side of the layer I as $S_e < S_{et}$ in this case (Figure 6b). As the ions traverse the film and slow down, they cross the threshold, S_{et}, and thus, nanopits are observed on the back side of layer I (Figure 6c). The nanopits on the back side of layer I (Figure 6c) and the front side of layer II (Figure 6d) are similar, in size and abundance, indicating that there is no apparent directionality effect of the projectiles on either the threshold or opening size distribution. The electron cascade due to momentum transfer from the incoming ions has a preferred forward direction that could result in a difference between the nanostructure formed on the exiting side of layer I and the entering side of layer II of the film. A thorough analysis of the comparison between them can be used to study the damage

mechanism involved. But, as most of the top layer of the film containing this information is removed by bulk etching in our case, such analysis of the damage mechanism is not carried out here. Further, as the ions traverse the second layer, they move away from S_{et}, where the etchable fraction of the track increases, and consequently, a larger number of nanopits are observed on the back side of layer II (Figure 6e).

The evolution of average pore diameter is studied for three different projectiles in the region (III), viz. 5 MeV Co^{3+}, 17 MeV Co^{7+}, and 37 MeV Co^{9+}, by analyzing the films etched for a time ranging from 15 min to 8 h. **Figure 7** shows a) a plot for change in pore diameter for these films as a function of etching time, where the error bars indicate the standard deviation of pore diameter distribution (based on 60–80 pores for $T_E \geq 1.5$ h and 10–30 pores for $T_E < 1.5$ h) for each etching time, along with

ADVANCED
SCIENCE NEWS
www.advancedsciencenews.com

Macro-
olecular
Materials and Engineering
Open Access
www.mame-journal.de

Figure 7. a) Change in pore diameter as a function of etching time (slope $= 2V_R$); SEM images of films irradiated with 37 MeV Co^{9+} and etched for b) 1 h, c) 3 h, and d) 8 h at 50 °C. The pore diameter increases with etching time.

Table 2. List of radial etch rates (V_R) for different projectiles for $T_E < 2$ h and $T_E \geq 2$ h.

Projectile Ion	S_e [keV nm^{-1}]	V_R for $T_E < 2$ h [nm h^{-1}]	V_R for $T_E \geq 2$ h [nm h^{-1}]
5 MeV Co^{3+}	1.91	1.7 ± 1.1	8.7 ± 0.8
(5 ± 0.3) MeV Co*	1.9 ± 0.1	3.9 ± 0.5	6.5 ± 0.8
17 MeV Co^{7+}	4.43	4.7 ± 0.7	8.1 ± 0.5
37 MeV Co^{9+}	5.55	6.4 ± 0.6	9.8 ± 0.7

*Average energy for the transmitted ions from 7.5 μm thick PI film, when irradiated with 37 MeV Co^{9+}, was determined by SRIM simulation.

SEM images of the front side of the films irradiated with 37 MeV Co^{9+} and etched for b) 1 h, c) 3 h, and d) 8 h. The average pore diameter is observed to increase with time. Two notes may be made about the initial opening phase of the pores based on the present data. First, extrapolating the observed pore radius to zero etch time yields a positive value of a few nm, which indicates the initial ion track radius. Second, the initial decreased pore growth rate (for $T_E < 2$ h) might be attributable to a less efficient wetting of the pore by the etchant due to a narrow pore opening at the beginning of the process. The radial etch rate (V_R) is defined as the rate of increase of pore radius with time and is calculated as half of the slope of the linearly fitted plots of average diameter as a function of T_E. **Table 2** gives V_R calculated separately for $T_E < 2$ h and $T_E \geq 2$ h. The V_R calculated for $T_E \geq 2$ h for different irradiation conditions is approximately the same suggesting that the pores, after the initial opening phase, grow radially at a rate of V_B. To substantiate or deny this claim, the bulk etch rate of the pristine films exposed to the same etching conditions was calculated using EBS. The V_R for the case of the transmitted ions at an average energy of 5 MeV is lower than in other cases observed here. This can be due to the fact that these transmitted ions (for the incoming ion of 37 MeV Co) have a distribution of energy, spreading them across the regions (II) and (III). Thus, the opening diameters on the back side can be either due to intermittent track or continuous track leading to a lower average opening diameter and relatively different V_R.

The EBS spectra for two pristine (labeled as Reference 1 and Reference 2) and four unirradiated but etched films are shown in
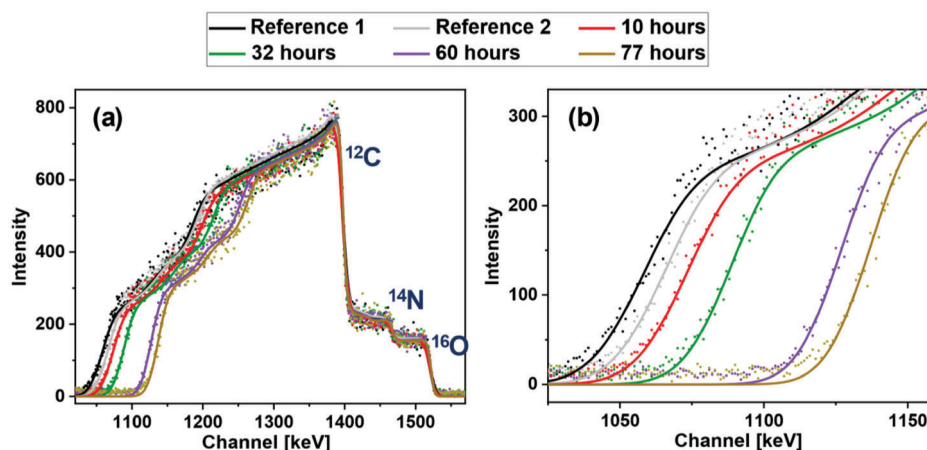
Figure 8a, with the magnified image of the trailing edge of the PI peak in Figure 8b. The thickness of the films was calculated by fitting the spectra with SIMNRA.[32] All the spectra fit well for the stoichiometric $C_{22}H_{10}N_2O_5$ (note, however, that the H fraction is not directly measured with this technique). The final thickness of the film is always calculated from the EBS spectrum while the initial thickness is calculated to be A) 7.6 ± 0.1 μm by taking an average of two reference PI films from EBS spectra and B) 7.5 ± 0.1 μm by measuring the weight and dimensions of the film before etching. **Figure 9** shows a plot of the thickness of the dissolved layer from the film after symmetrical etching as a function of etching time (slope $= 2V_B$). As the film is etched from both sides, V_B is equal to half of the slope of graphs, and is calculated to be $\approx$10.5 ± 0.4 nm h^{-1} using method (A) and 10.1 ± 0.3 nm h^{-1} using method (B). These V_B values are comparable to V_R observed for different projectiles for $T_E \geq 2$ h (Table 2) verifying that after a fast, initial removal of the narrow ion track core (a few nm wide and not directly resolved in this work), the pores grow by etching of undamaged PI at a near bulk etch rate. Also, comparing this V_B value of 10.3 ± 0.4 nm h^{-1} and the size of the pore opening (diameter $\approx$ 55 ± 10 nm, for 4 h etching) with the charge state equilibration length (d) of 5 ± 2 nm, further verifies our assumption that effect of q_{in} being different from q_{eq} is minimal in this work.

A cross-section of the etched-out pores for a film irradiated with 37 MeV Co^{9+} and etched for 4 h at 50 °C is also investigated using TEM. **Figure 10** shows the TEM cross-section images while Figure 5c,f contains the SEM images of the front and back sides respectively of the same film. Figure 10 shows a) $\approx$4 μm long continuous cylindrical pore, with an opening toward the ion beam facing side of the membrane; the magnified images of b) a nanopore opening at the ion-beam facing side of the membrane, c) part of the track in the middle of the film, and d) a nanopit with depth on the order of 100 nm observed on the back side of the membrane. A V_T on the order of 1 μm h^{-1} can be calculated by dividing the length of the observed continuous pore ($\approx$4 μm) by the time for which the film was etched (4 h). However, it cannot be excluded that the pore was cut across while preparing the lamella, and thus, only a part of this pore is observed (given that the range of 37 MeV ^{59}Co ions is $\approx$11.5 μm). Even if this were to be the case, V_T of $\approx$1 μm h^{-1} could be considered as a lower limit estimate of an average track etch rate.

4. Summary and Concluding Remarks

Nanopore formation in polyimide films was investigated by chemically etching the ion tracks formed upon irradiation with MeV energy ions. For the studied Kapton 30EN polyimide films, two velocity-dependent thresholds in terms of electronic stopping power (S_e), *viz.* S_{et} and S_{et}^c, are observed for the formation of intermittent and continuous tracks respectively. Incoming ions should have S_e above the S_{et}^c (region (III) in Figure 4) to form continuous tracks that are characterized by a small distribution in the pore opening diameter upon etching of the ion tracks (Figure 2g). The lowest observed value for S_{et}^c in the present work is 1.4 ± 0.1 keV nm^{-1}, for projectile ions with energy $\approx$0.07 MeV u^{-1}. Intermittent tracks are formed in the region where $S_{et} < S_e < S_{et}^c$, leading to a wide distribution in the opening diameter upon etching of the ion tracks (Figure 2e,f). Below S_{et}, no openings on

**ADVANCED
SCIENCE NEWS**

www.advancedsciencenews.com

acro-
olecular
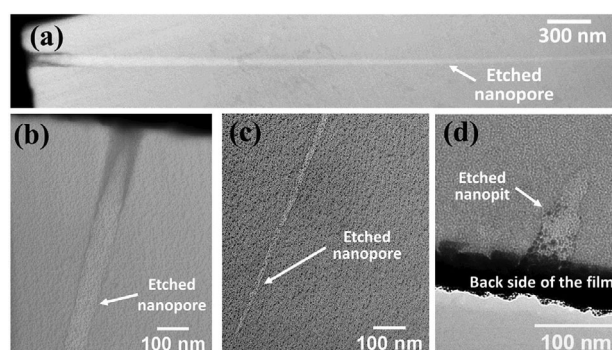**Materials and Engineering**
Open Access

www.mame-journal.de

Figure 8. a) EBS spectra for the pristine and etched PI film and b) Magnified EBS spectra for the trailing edge of the PI peak. Experimental spectra are represented by dots and SIMNRA-fitted spectra are represented by lines.
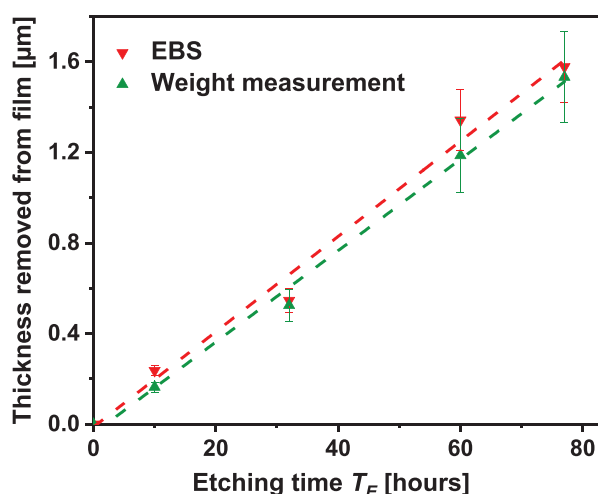
Figure 9. Thickness of the PI film removed after symmetrical etching (slope = $2V_B$) as a function of etching time. The initial thickness of the films is calculated by: (▼) taking an average of two reference PI films from EBS spectra (the dominant error in measuring thickness from EBS spectrum is from S_e used to simulate the spectrum in SIMNRA), and (▲) measuring the weight and dimensions of the films before etching (the error is calculated from the uncertainty in the measurement of mass and area of the film).

Figure 10. a) TEM cross-section image of the ≈4 µm long etched nanopore with the opening on the beam facing/front side of the film. Magnified TEM cross-section images of b) a nanopore at the beginning of the front side; c) in the middle of the film; and d) ≈100 nm long etched pit with an opening on the back side of the film. The film was irradiated with 37 MeV Co^{9+} and etched for 4 h at 50 °C.

the surface corresponding to etchable tracks in the films are observed. The lowest observed value for S_{et}, in the present work, is 0.5 ± 0.2 keV nm^{-1} for projectile ions with energy 0.02 MeV u^{-1} and increases to 1.2 ± 0.1 keV nm^{-1} for ions with energy 1.0 MeV u^{-1}, indicating velocity effect (cf. 1.85 keV nm^{-1} for high-velocity ions as reported in reference [20]). As indicated in Figure 4, the velocity effect becomes less dominant in the S_{et} for SHI irradiation. The velocity effect is also observed in $S_{et}{}^c$ for low energy projectile ions ($E < 1$ MeV u^{-1}), where it increases from (1.4 ± 0.1) to (1.8 ± 0.2) keV nm^{-1}, for the ions with energy ranging from 0.07 to 0.3 MeV u^{-1}.

The material bulk etch rate, V_B, is calculated to be 10.3 ± 0.4 nm h^{-1} by measuring the change in the film thickness with etching time (T_E) from EBS spectra. A lower limit to the track etch

rate, V_T, was estimated at ≈1 µm h^{-1} by measuring the length of a pore etched from a continuous ion track formed by irradiating the film with projectiles lying in the region (III). The pore cross section depends on many other parameters. As a matter of fact, V_T needs to be measured by other techniques. In this work, V_T is estimated for one projectile ion (37 MeV $^{59}Co^{9+}$) to compare it to V_B. V_T, in this case, is ≈100 times higher than V_B and the radial increase of pore size in region (III) is comparable to V_B. For intermittent tracks, the etchable part is dissolved with V_T but the rest of the "track" material is removed with V_B leading to an average etch rate equal to a weighted sum of the V_T and V_B. The effective initial ion track radius, measured here by extrapolating the observed time evolution of pore radii to zero etch time, is estimated as 2–4 nm, which is also in agreement with reported results in the literature.[21,39] The effective ion track core is relatively rapidly dissolved at a rate characterized by V_T at the beginning of the etching process and then the pores keep on growing with the bulk etch rate for the rest of the etching time.

We expect that the ability to produce nanopores using ions in the MeV energy range, which are more accessible than SHI, will prove helpful in the research and also, in bringing the

commercialization of solid-state nanoporous devices closer to practical reality. Thus, we claim that medium-sized ion accelerator infrastructures, in particular tandem machines or small cyclotrons, with the ability to deliver these ions are suitable for the production of ion track membranes. Out of the ion beams used in this work, some featured high enough energies (e.g., 16 MeV ^{16}O, 37 MeV ^{59}Co, and 42 MeV ^{197}Au) to penetrate through the investigated 7.5 µm thick PI films, whereas others did not (e.g., 11 MeV ^{28}Si, 9 MeV ^{59}Co, and 12 MeV ^{197}Au). For applications where pores penetrating through the fabricated membrane are of interest, the maximal available ion energy will set an upper limit to the membrane thickness. However, for certain applications such as ion separation and filtration, thinner porous membranes are preferred as they are reported to have better performance.[1] In such cases, a longer range of GeV ions does not give any advantage over MeV ions. On the other hand, the accessibility of MeV ions in the industry gives them an edge over GeV ions. The possibility to produce nanopores in PI using MeV energy ions and the excellent properties of the PI films can open up new opportunities for the development of polyimide-based devices for different possible applications.

Conflict of Interest

The authors declare no conflict of interest.

Data Availability Statement

The data that support the findings of this study are available from the corresponding author upon reasonable request.

[1] P. Wang, M. Wang, F. Liu, S. Ding, X. Wang, G. Du, J. Liu, P. Apel, P. Kluth, C. Trautmann, Y. Wang, *Nat. Commun.* **2018**, *9*, 569.

[2] Q. Wen, D. Yan, F. Liu, M. Wang, Y. Ling, P. Wang, P. Kluth, D. Schauries, C. Trautmann, P. Apel, W. Guo, G. Xiao, J. Liu, J. Xue, Y. Wang, *Adv. Funct. Mater.* **2016**, *26*, 5796.

[3] A. Mara, Z. Siwy, C. Trautmann, J. Wan, F. Kamme, *Nano Lett.* **2004**, *4*, 497.

[4] O. A. Saleh, L. L. Sohn, *Nano Lett.* **2003**, *3*, 37.

[5] W. Yan, V. K. S. Hsiao, Y. B. Zheng, Y. M. Shariff, T. Gao, T. J. Huang, *Thin Solid Films* **2009**, *517*, 1794.

[6] D. Cohen-Tanugi, J. C. Grossman, *Nano Lett.* **2012**, *12*, 3602.

[7] D. Kaya, K. Keçeci, *J. Electrochem. Soc.* **2020**, *167*, 037543.

[8] Z. Siwy, L. Trofin, P. Kohli, L. A. Baker, C. Trautmann, C. R. Martin, *J. Am. Chem. Soc.* **2005**, *127*, 5000.

[9] S. Tan, D. Gu, H. Liu, Q. Liu, *Nanotechnology* **2016**, *27*, 155502.

[10] S. Garaj, W. Hubbard, A. Reina, J. Kong, D. Branton, J. A. Golovchenko, *Nature* **2010**, *467*, 190.

[11] I. Vlassiouk, P. Y. Apel, S. N. Dmitriev, K. Healy, Z. S. Siwy, *Proc. Natl. Acad. Sci. U. S. A.* **2009**, *106*, 21039.

[12] N. Hegedüs, K. Balázsi, C. Balázsi, *Materials* **2021**, *14*, 5658.

[13] L. A. Vlasukova, F. F. Komarov, V. N. Yuvchenko, O. V. Mil'chanin, A. Y. Didyk, V. A. Skuratov, S. B. Kislitsyn, *Bull. Russ. Acad. Sci.: Phys.* **2012**, *76*, 582.

[14] E. Y. Kaniukov, J. Ustarroz, D. V. Yakimchuk, M. Petrova, H. Terryn, V. Sivakov, A. V. Petrov, *Nanotechnology* **2016**, *27*, 115305.

[15] F. Liu, M. Wang, X. Wang, P. Wang, W. Shen, S. Ding, Y. Wang, *Nanotechnology* **2019**, *30*, 052001.

[16] K. V. R. Sidhikku, N. Ghasem, M. Al-Marzouqi, *J. Ind. Eng. Chem.* **2021**, *98*, 103.

[17] P. Y. Apel, *Radiat. Phys. Chem.* **2019**, *159*, 25.

[18] Y. Wang, Q. Yang, Z. Wang, *Front. Genet.* **2015**, *5*, 449.

[19] Z. Siwy, D. Dobrev, R. Neumann, C. Trautmann, K. Voss, *Appl. Phys. A: Mater. Sci. Process.* **2003**, *76*, 781.

[20] C. Trautmann, S. Bouffard, R. Spohr, *Nucl. Instrum. Methods Phys. Res. B* **1996**, *116*, 429.

[21] T. Yamauchi, K. Matsukawa, Y. Mori, M. Kanasaki, A. Hattori, Y. Matai, T. Kusumoto, A. Tao, K. Oda, S. Kodaira, T. Konishi, H. Kitamura, N. Yasuda, R. Barillon, *Appl. Phys. Express* **2013**, *6*, 046401.

[22] S. Metz, C. Trautmann, A. Bertsch, P. Renaud, *J. Micromech. Microeng.* **2004**, *14*, 324.

[23] C. Trautmann, W. Brüchle, R. Spohr, J. Vetter, N. Angert, *Nucl. Instrum. Methods Phys. Res. B* **1996**, *111*, 70.

[24] L. Klintberg, M. Lindeberg, G. Thornell, *Nucl. Instrum. Methods Phys. Res. B* **2001**, *184*, 536.

[25] E. A. Heins, Z. S. Siwy, L. A. Baker, C. R. Martin, *Nano Lett.* **2005**, *5*, 1824.

[26] P. Ström, D. Primetzhofer, *J. Instrum.* **2022**, *17*, P04011.

[27] J. F. Ziegler, M. D. Ziegler, J. P. Biersack, *Nucl. Instrum. Methods Phys. Res. B* **2010**, *268*, 1818.

[28] G. Schiwietz, P. L. Grande, *Nucl. Instrum. Methods Phys. Res. B* **2001**, *175–177*, 125.

[29] P. Ström, D. Primetzhofer, *Phys. Rev. A* **2021**, *103*, 022803.

[30] I. M. Kolthoff, E. B. Sandell, *Textbook of Quantitative Inorganic Analysis*, 3rd ed., Macmillan, London **1952**.

[31] M. W. Lister, *Can. J. Chem.* **1956**, *34*, 465.

[32] M. Mayer, SIMNRA User's Guide, Report IPP 9/113, Max-Planck-Institut für Plasmaphysik, Garching, Germany **1997**.

[33] C. A. Schneider, W. S. Rasband, K. W. Eliceiri, *Nat. Methods* **2012**, *9*, 671.

[34] D. Nečas, P. Klapetek, *Open Phys.* **2012**, *10*, 181.

[35] M. Toulemonde, C. Trautmann, E. Balanzat, K. Hjort, A. Weidinger, *Nucl. Instrum. Methods Phys. Res. B* **2004**, *216*, 1.

[36] A. Meftah, F. Brisard, J. M. Costantini, M. Hage-Ali, J. P. Stoquert, F. Studer, M. Toulemonde, *Phys. Rev. B* **1993**, *48*, 920.

[37] R. Kaur, P. Ström, D. Primetzhofer, *Nucl. Instrum. Methods Phys. Res. B* **2023**, *536*, 132.

[38] Y. Y. Wang, C. Grygiel, C. Dufour, J. R. Sun, Z. G. Wang, Y. T. Zhao, G. Q. Xiao, R. Cheng, X. M. Zhou, J. R. Ren, S. D. Liu, Y. Lei, Y. B. Sun, R. Ritter, E. Gruber, A. Cassimi, I. Monnet, S. Bouffard, F. Aumayr, M. Toulemonde, *Sci. Rep.* **2015**, *4*, 5742.

[39] Y. Sun, C. Zhang, Z. Zhu, Z. Wang, Y. Jin, J. Liu, Y. Wang, *Nucl. Instrum. Methods Phys. Res. B* **2004**, *218*, 318.